Report

Neuron

Principles of Synaptic Organization of GABAergic Interneurons in the Striatum

Highlights

- Optogenetic control reveals connectivity of striatal FS and LTS interneurons
- FSIs form short-range and LTSIs form long-range connections within the striatum
- FSIs and LTSIs target proximal and distal dendritic regions, respectively

Authors

Christoph Straub, Jessica Lizette Saulnier, Aurelien Bègue, Danielle D. Feng, Kee Wui Huang, Bernardo Luis Sabatini

Correspondence

bernardo_sabatini@hms.harvard.edu

In Brief

Straub et al. dissect the microcircuitry of two classes of interneurons in the striatum. They show subtype-specific synaptic organization at both cellular and subcellular levels despite the apparently random and unlayered organization of their target cells.

Straub et al., 2016, Neuron *92*, 84–92
October 5, 2016
http://dx.doi.org/10.1016/j.neuron.2016.09.007

CellPress

CellPress

Neuron
Report

Principles of Synaptic Organization of GABAergic Interneurons in the Striatum

Christoph Straub,[1] Jessica Lizette Saulnier,[1] Aurelien Bègue,[1] Danielle D. Feng,[1] Kee Wui Huang,[1] and Bernardo Luis Sabatini[1,2,*]

[1]Howard Hughes Medical Institute, Department of Neurobiology, Harvard Medical School, 220 Longwood Ave., Boston, MA 02115, USA
[2]Lead Contact
*Correspondence: bernardo_sabatini@hms.harvard.edu
http://dx.doi.org/10.1016/j.neuron.2016.09.007

SUMMARY

The striatum, the entry nucleus of the basal ganglia, lacks laminar or columnar organization of its principal cells; nevertheless, functional data suggest that it is spatially organized. Here we examine whether the connectivity and synaptic organization of striatal GABAergic interneurons contributes to such spatial organization. Focusing on the two main classes of striatal GABAergic interneurons (fast-spiking interneurons [FSIs] and low-threshold-spiking interneurons [LTSIs]), we apply a combination of optogenetics and viral tracing approaches to dissect striatal microcircuits in mice. Our results reveal fundamental differences between the synaptic organizations of both interneuron types. FSIs target exclusively striatal projection neurons (SPNs) within close proximity and form strong synapses on the proximal somatodendritic region. In contrast, LTSIs target both SPNs and cholinergic interneurons, and synaptic connections onto SPNs are made exclusively over long distances and onto distal dendrites. These results suggest fundamentally different functions of FSIs and LTSIs in shaping striatal output.

INTRODUCTION

In many brain regions, including retina, cerebellum, cortex, and hippocampus, projection neurons and interneurons, as well as their synaptic connections, are organized into laminae along the basal-apical axis of the principal neurons (e.g., Druckmann et al., 2014; Ito, 2006; Sanes and Zipursky, 2010). This structure reflects an organization into distinct signaling domains, both at subcellular and circuit levels (DeFelipe et al., 2002; London and Häusser, 2005). For example, at the circuit level, cortical layer 2/3 pyramidal neurons receive information from layer 4 while influencing neighboring regions via long-range lateral projections (Harris and Shepherd, 2015). At the subcellular level, dendritic-targeting interneurons regulate excitability and plasticity, whereas somatic-targeting interneurons control spiking and synchronize functional assemblies of active principal neurons (Roux and Buzsáki, 2015).

Whether such spatial organization of synapses exists in structures that lack laminae or columns is unclear. One such structure is the striatum, the entry point for most excitatory projections to the basal ganglia, a subcortical group of nuclei important for the generation of purposeful movements. Striatal projection neurons (SPNs) lack apical-basal structure, extend dendrites radially, and appear randomly oriented and interconnected (Kawaguchi et al., 1990). There are only small differences in the proximal-distal dendritic organization of excitatory inputs (MacAskill et al., 2012; Plotkin et al., 2011) and no discernible patterns in the structure of SPN-to-SPN inhibitory synapses. Thus, with the exception of the separation into patch and matrix compartments, there is no anatomical evidence for spatial organization in the striatum. Nevertheless, SPNs are active in dynamically organized, competing functional assemblies (Bakhurin et al., 2016; Redgrave et al., 2011), suggesting the existence of microcircuits that underlie such spatial ensembles.

In other regions, GABAergic interneurons can guide the formation of functional assemblies (Roux and Buzsáki, 2015). Interneurons account for only 5% of all neurons in the striatum, but they are essential for striatal function (Gittis and Kreitzer, 2012). Three main classes of striatal interneurons are classically recognized: cholinergic interneurons (CINs), somatostatin (SST)-positive low-threshold-spiking interneurons (LTSIs), and parvalbumin (PV)-positive fast-spiking GABAergic interneurons (FSIs) (Kawaguchi, 1993). Paired recordings between SPNs and interneurons have revealed the connectivity among different cell classes (Gittis et al., 2010; Koos et al., 2004) but have not illuminated the spatial organization of synaptic inputs.

Here we characterize the spatial organization of the striatal microcircuit formed by LTSIs and FSIs and their respective targets. We find different target selection and synaptic patterns for the two types of GABAergic interneurons, with FSIs forming strong synapses onto the proximal somatodendritic region of nearby SPNs, whereas LTSIs target both SPNs and CINs and form synapses onto SPNs over long distances and onto distal dendrites. The results help define the microcircuits formed by LTSIs and FSIs and imply fundamentally different roles for the two interneuron types in controlling striatal activity.

RESULTS

To gain precise and selective optogenetic control over LTSIs and FSIs, we virally delivered cre-dependent channelrhodopsin-2 (ChR2) into the striatum of SST-cre and PV-cre mice,

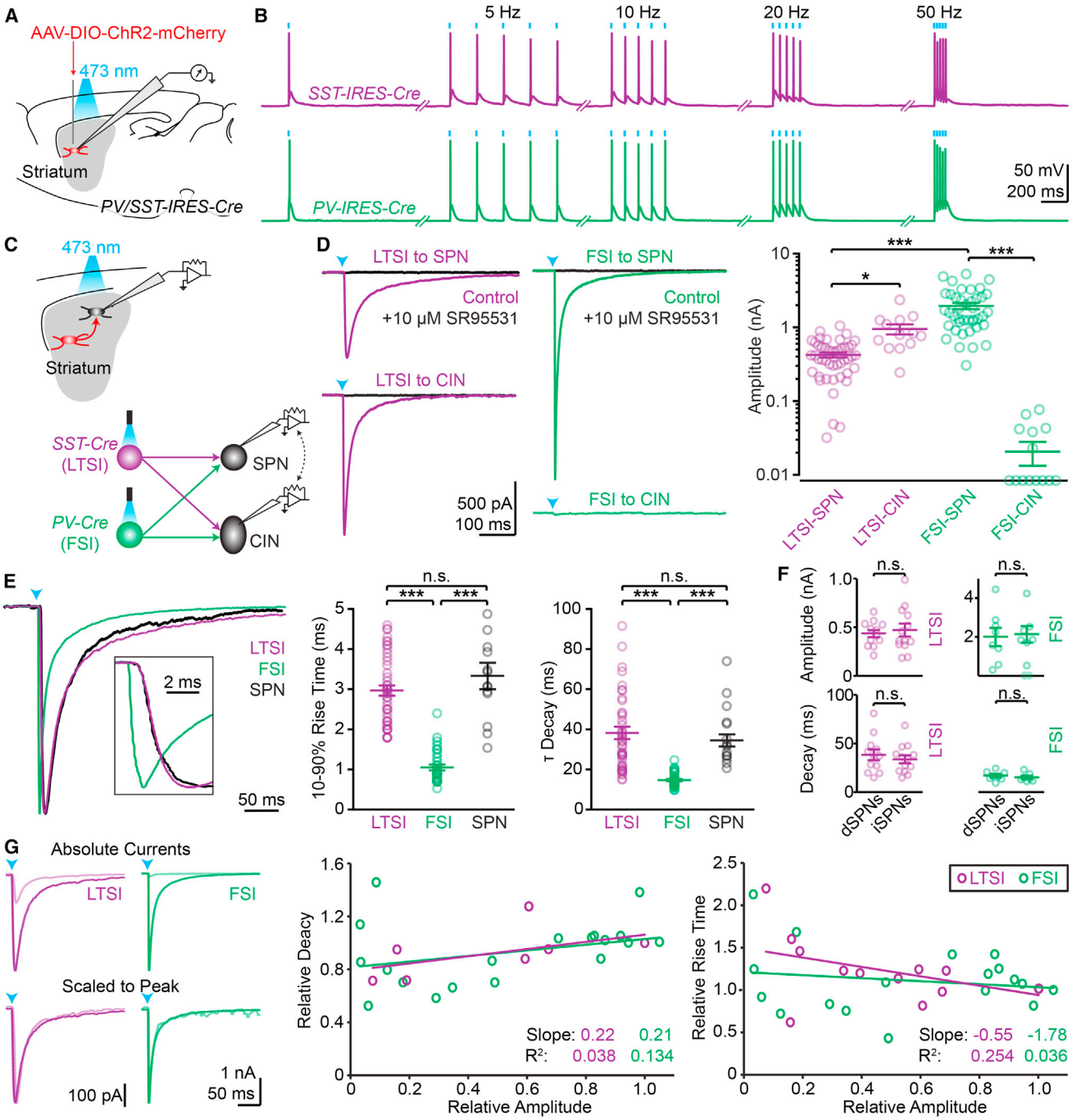

Figure 1. Optogenetic Control of LTSIs and FSIs Reveals Interneuron Connectivity

(A and B) ChR2 was virally expressed in SST (labeling LTSIs) or PV-positive (labeling FSIs) cells in the striatum (A) and allowed faithful optical control of spiking activity (B). Blue ticks indicate optical stimuli.

(C) The outputs of LTSIs and FSIs were examined by recording from ChR2-negative SPNs and CINs.

(D) Representative examples of synaptic currents (left; arrowheads: light stimulus) and summary of IPSC amplitudes (right).

(E) Representative examples of synaptic currents in SPNs from LTSIs (magenta), FSIs (green), or SPNs (black) scaled to peak (left). Inset shows rising phase on extended time scale. Quantification of 10%–90% rise time (middle) and decay time constants (right) across all cells.

(F) No differences in IPSC amplitude (top) or decay kinetics (bottom) were found in direct (dSPNs) and indirect (iSPNs) pathway SPNs.

(legend continued on next page)

respectively (Figures 1A and 1B; Figures S1G and S1H). We avoided crossing cre-lines with floxed ChR2-mice, since this labels non-SST-expressing cells in the striatum of SST-cre mice (Figure S1). To determine postsynaptic targets, we recorded from ChR2-negative cells in acute slices (Figure 1C), identifying SPNs and CINs morphologically and electrically (Figures S1C–S1G; Straub et al., 2014). Activation of LTSIs triggered reliable inhibitory postsynaptic currents (IPSCs) in SPNs and CINs, with larger amplitudes in the latter (423 ± 32 pA, n = 46 cells from 14 mice and 951 ± 51 pA, n = 13/6; $p < 0.05$). In contrast, FSIs triggered large IPSCs in SPNs but did not evoke appreciable currents in CINs (1,965 ± 193 pA, n = 41/15 and 21 ± 7 pA, n = 14/6; $p < 0.001$; Figure 1D). Independent of amplitude, rise and decay times were fast for optically evoked FSI IPSCs and slower for LTSI IPSCs (LTSI: 10%–90% rise time 3.0 ± 0.1 ms, decay time constant 38 ± 3.1 ms; n = 46/14; FSI: rise time 1.1 ± 0.1 ms, decay time 14.4 ± 0.5 ms; n = 41/15; each $p < 0.0001$; Figures 1E and 1G). Evoked IPSCs from either interneuron type in direct and indirect pathways were similar (amplitude: LTSI to dSPN 438 ± 37 pA [n = 12/4], to iSPN 475 ± 67 pA [n = 13/4], p = 0.94; FSI to dSPN 2,003 ± 475 pA [n = 8/4], to iSPN 2,153 ± 424 pA [n = 9/4], p = 0.87. Decay: LTSI to dSPN 38.3 ± 5.5 ms, to iSPN 33.8 ± 4.1 ms, p = 0.57; FSI to dSPN 16.8 ± 1.7 ms, to iSPN 15.1 ± 1.6 ms, p = 0.4; Figure 1F).

The strong, but selective, connectivity of FSIs onto SPNs had been described in paired-recording studies, but the same approach failed to detect postsynaptic targets of LTSIs (Gittis et al., 2010; Szydlowski et al., 2013). This discrepancy is not due to the different labeling strategies (Figures S1K and S1L), but might rather arise from experimental differences. Paired recordings probe unitary synaptic responses, which may be too small for reliable detection. Moreover, paired recordings are typically obtained from cells in close proximity (<250 μm apart in Gittis et al., 2010), and it is possible that LTSIs do not reliably form synapses onto nearby SPNs (Ibáñez-Sandoval et al., 2011). By contrast, optogenetic stimulation simultaneously recruits many opsin-expressing presynaptic axons within the field of view, irrespective of the distance of the transfected cells.

We tested whether individual LTSI inputs generate synaptic currents >20 pA (the detection threshold in Gittis et al., 2010, with similar recording conditions). Strontium-evoked desynchronized release (Xu-Friedman and Regehr, 1999) revealed unitary amplitudes of 37 ± 1 pA (n = 6/3) and 57 ± 2 pA (n = 5/3; $p < 0.0001$, Kolmogorov-Smirnov test) for LTSIs and FSIs, respectively (Figures 2A–2E). Similar to compound IPSCs, strontium-evoked unitary IPSCs from LTSIs had slower decay times than from FSIs (LTSI: 7.8 ± 1 ms, n = 6/3; FSI: 4.5 ± 0.4 ms, n = 5/3; $p < 0.05$; Figures 2C and 2D). Using a minimal stimulation paradigm, LTSI unitary amplitudes (31 ± 1 pA, n = 7/3; Figures 2F–2H) were confirmed to be above detection threshold.

In the original classification by Kawaguchi, LTSI axons are described as running "in straight lines…. extending more than 1 mm" (Kawaguchi, 1993). To test whether this finding is general and whether it reflects the distribution of synaptic LTSI connections, we used a viral *trans*-synaptic labeling approach (Figure 3; Figure S2). Cre-dependent infection with rabies virus was targeted to a small group of direct-pathway SPNs in central dorsal striatum (Figure 3A). Post hoc immunohistochemical identification of LTSIs or FSIs and serial reconstruction of the striatum allowed mapping of the position of each starter cell (SPN) and monosynaptically connected interneuron (Figures 3A–3C). On average, ~50 starter cells were transfected in each experiment (range: 5–152), spread over an ~500-μm-diameter volume (all experiments combined: LTSIs full-width half-maximum (FWHM) x/y/z: 606/410/260 μm; FSIs: 657/549/406 μm). The positions of putatively connected interneurons of each type were different: LTSIs were dispersed several millimeters around the starter cells, whereas all FSIs were within close proximity of starter cells (Figure 3D). The distances between individual labeled LTSI and the closest starter cell were further than 250 μm (570 ± 59 μm, n = 54/4), whereas all labeled FSIs were near a starter cell (123 ± 25 μm, n = 24/4; $p < 0.0001$; Figure 3E). This fundamentally different organizing principle of FSIs and LTSIs explains why synaptic connections between LTSIs and SPNs are difficult to measure with paired recordings.

In cortex and hippocampus, PV- and SST-positive interneurons target proximal and distal dendrites, respectively, leading to differential dendritic filtering and synaptic current kinetics (e.g., Marlin and Carter, 2014; Stefanelli et al., 2016). Since IPSCs from LTSIs were consistently slower than from FSIs (Figures 1E, 2C, and 2D), we asked whether this synaptic organization is conserved in the unlayered striatum. Electron microscopy studies find PV-positive synapses to be enriched on somata (Bennett and Bolam, 1994) or evenly distributed along dendrites (Kita et al., 1990; Kubota and Kawaguchi, 2000). SST-positive terminals are described more consistently as enriched on dendrites (DiFiglia and Aronin, 1982; Kubota and Kawaguchi, 2000), but the quantitative distribution of the two input types along the somatodendritic compartment of SPNs remains unknown.

To determine the subcellular distribution of synaptic inputs onto SPNs, we attempted to map the location of individual synapses by restricting ChR2 activation to a small presynaptic volume and drive neurotransmitter release onto a visualized dendritic portion. We used temporal focusing (TF) to expand the laser spot for two-photon (2P) excitation in the xy plane while preserving z resolution (Zhu et al., 2005), effectively forming a small disc of light that could be positioned onto any region of interest (Figure S4; Table S1). The illumination spot (940 nm) had a diameter of ~10 μm, resulting in a 2P-activation profile of ChR2 in scattering tissue with an FWHM of ~25 μm (Figures S4B–S4G). We alternated one-photon (1P) wide-field stimulation (1 ms) and 2P TF-spot activation (10 ms) on multiple locations over the recorded SPNs to stimulate ChR2 expressed in FSIs

(G) Example traces of IPSCs in SPNs from LTSIs (magenta) or FSIs (green) (left). Reducing light for ChR2 activation reduced the amplitude (top; light colored traces) but did not affect the kinetics (bottom). The decay (middle) and rising (right) kinetics for LTSI (n = 5 cells) and FSI (n = 4) inputs were relatively independent of and poorly explained by relative current amplitude.

Bar diagrams represent mean ± SEM; n.s., not significant, *$p < 0.05$, ***$p < 0.001$.

See also Figure S1.

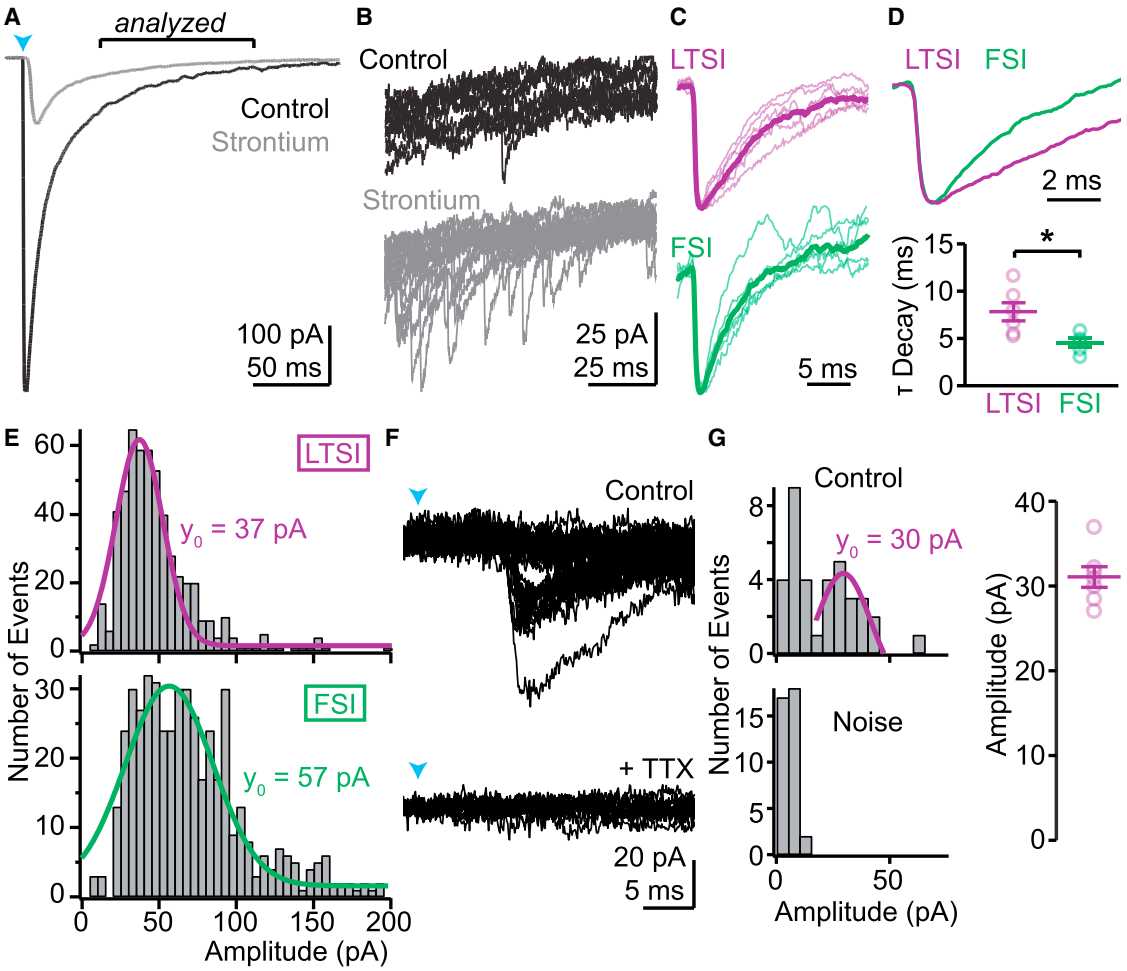

Figure 2. Unitary Responses of LTSIs Are above Detection Threshold

(A) Average traces under control conditions (black) and after replacing external calcium by strontium (gray), which desynchronizes fusion of neurotransmitter-containing vesicles.

(B) Overlay of ten traces from the period indicated in (A) reveals numerous small events in strontium, reflecting delayed individual vesicular release events following optogenetic activation.

(C) Unitary responses in strontium scaled to peak for LTSIs (magenta) and FSIs (green). Thin lines indicate average waveform from individual cells, and thick lines indicate averages for cell types.

(D) Top: overlay of average LTSI and FSI unitary events shows a slower decay for LTSI currents. Bottom: summary for all cells.

(E) Amplitude distribution of synaptic events 50–150 ms post-stimulus for LTSIs (top, magenta; n = 6/3) and FSIs (bottom, green: n = 5/3). Gaussian fits (lines) indicate median event sizes of 37 and 57 pA, respectively.

(F) Examples of evoked currents following minimal ChR2 stimulation of LTSIs. Laser power was reduced (~0.2 mW/mm^2) and moved away from the recording site (390 μm) until failures appeared. The remaining currents were TTX sensitive (bottom) and had discrete minimal amplitudes, presumably reflecting unitary events.

(G) The distribution of amplitudes shows a clear peak above noise with median of ~30 pA in this example (left) and in 7 cells/3 mice (right).

Bar diagrams represent mean ± SEM; *p < 0.05.

or LTSIs (Figures S3A–S3D). The experiments were performed in tetrodotoxin/4-aminopyridine (TTX/4-AP) to restrict activation to presynaptic sites that are directly within the illumination spot (Petreanu et al., 2009).

This approach revealed inputs from FSIs onto the somatic regions of SPNs in every connected cell (n = 7/3, amplitude: 36% ± 12% of wide-field stimulation), but not onto dendritic locations (>50 μm from the cell body, n = 19 locations, 7 cells; Figures S3A and S3B). In contrast, no somatic input was found for LTSIs (n = 13/4), but one dendritic input location (141 μm from soma) was identified (out of 131 tested locations, 13 cells; Figures S3C–S3E). Given the efficient ChR2-mediated release from LTSI neurons even in TTX (76% ± 6% of control, data not shown), these results support that FSIs, but not LTSIs, form somatic synapses onto SPNs. However, given the low success rate of stimulating dendritic sites, no conclusions can be drawn about presence of dendritic synapses.

As an alternative method to determine the dendritic distance of synaptic inputs onto individual SPNs, we established whole-cell voltage-clamp recordings and performed voltage-jump

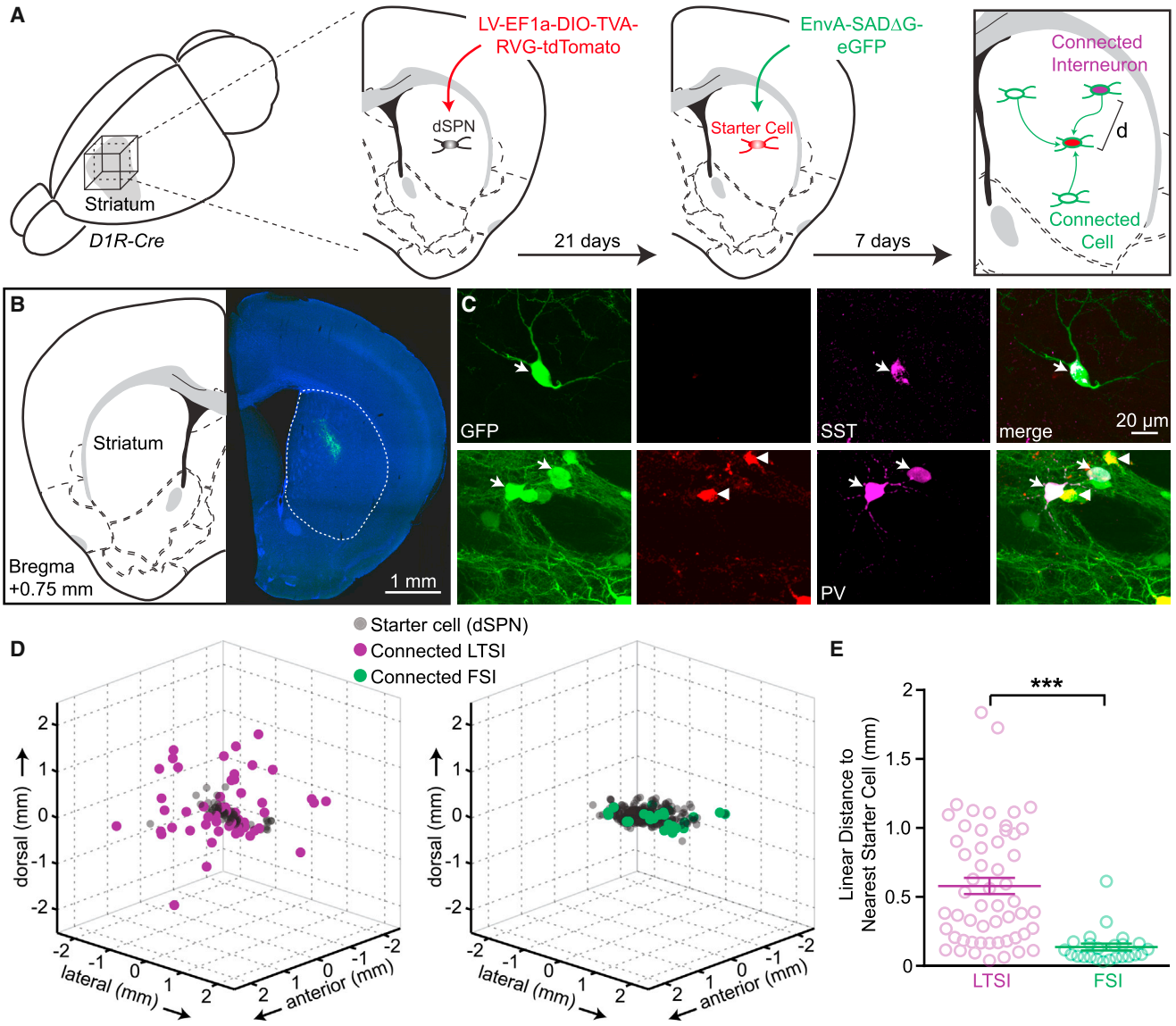

Figure 3. LTSIs Target Distant Postsynaptic Cells

(A) Experimental schematic: a small amount of a cre-dependent lentivirus encoding TVA receptor, rabies virus glycoprotein (RVG), and tdTomato was injected into the central dorsal striatum of *Drd1a-cre* mice, labeling a small population of dSPNs as starter cells (red). Pseudotyped rabies virus encoding for EGFP (green) was injected 3 weeks later into the same site, labeling starter cells (tdTomato and GFP co-expression) and monosynaptically connected cells (GFP only). Immunohistochemistry against SST or PV (magenta) identified monosynaptically connected LTSIs or FSIs, respectively, and the distance (d) between each connected interneuron and the closest starter cell was determined in three dimensions.

(B) Coronal section from a *Drd1a-cre* mouse showing rabies-virus expression (green) around the injection site in dorsal striatum (right) and corresponding atlas section 0.75 mm anterior of Bregma (left).

(C) Representative images of *trans*-synaptically labeled LTSI (arrows, top) or FSIs (bottom). Labeled FSIs were usually central to the injection site, in close proximity to starter cells (arrowheads), whereas connected LTSIs were frequently found distant from the injection sites as isolated GFP-positive cells.

(D) Three-dimensional representation of all connected cells identified as LTSIs (left) or FSIs (right). Data are from four independent experiments for each condition aligned by the center of mass of the starter cells. The spherical representation of individual cells is for display purposes and over-represents size of cells.

(E) The distances from each connected interneuron to the closest starter SPN are greater for LTSIs (magenta) than for FSIs (green). Bar diagram represents mean ± SEM; ***$p < 0.001$.

See also Figure S2.

experiments (Pearce, 1993). This approach relies on holding a cell at the reversal potential for the conductance examined while opening the channel (here: chloride passing through $GABA_A$ receptors) and then stepping the holding potential to a different value (Figures 4A and 4B). The onset kinetics of the resulting non-capacitive current are determined by the speed at which

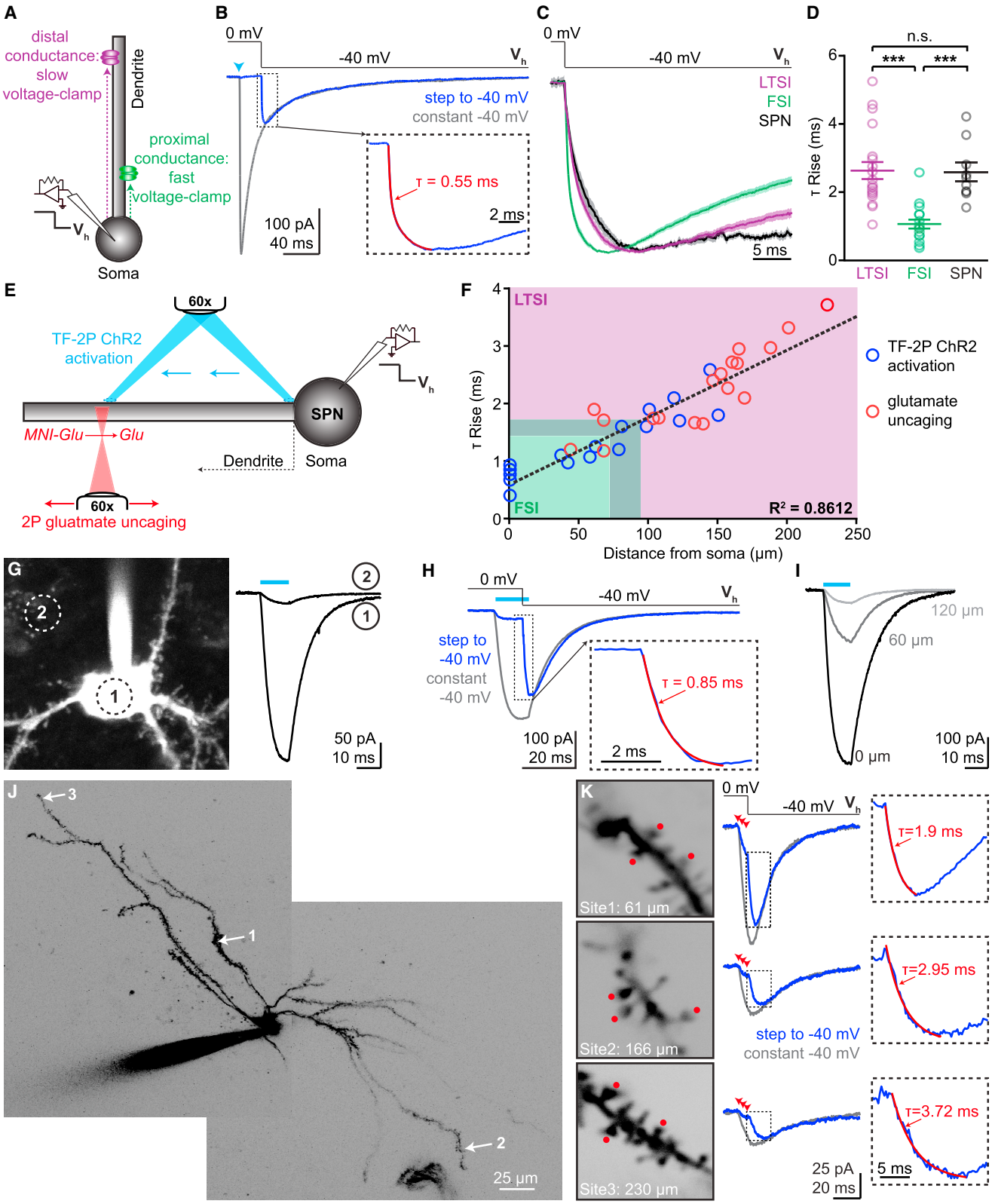

(legend on next page)

the conductance can be clamped to a new potential and are independent of channel activation kinetics. With all other factors being equal, conductances more distant from the somatic recording electrode will be clamped more slowly (Figure 4A). Applying this approach to SPNs following optogenetically triggered IPSCs revealed significantly slower onset of voltage-jump-evoked currents during LTSI-mediated IPSCs than during FSI-mediated IPSCs (LTSI: 2.7 ± 0.3 ms, n = 20/5; FSI: 1.1 ± 0.1 ms, n = 17/5, $p < 0.001$; Figures 4C and 4D). We repeated the experiments for SPN-to-SPN collateral synapses, which are known to target distal dendrites (Koos et al., 2004). The IPSC rise and decay kinetics from iSPNs to dSPNs were comparable to those of LTSI inputs but slower than FSI inputs (rise time 3.3 ± 0.3 ms, decay time 34.8 ± 3.1 ms; n = 13/4; Figure 1E). Similarly, current onset kinetics in voltage-jump experiments were slow for IPSCs originating from SPNs (2.5 ± 0.3 ms, n = 10/4; Figures 4C and 4D). Together, these results demonstrate that FSIs form synapses onto the proximal somatodendritic compartment of SPNs, whereas LTSIs target more distal regions. These findings indicate that the proximal-distal distribution of different GABAergic inputs is conserved even in a brain region where the principal cells are not arranged in layers and their dendrites do not form different macroscopic compartments.

In order to translate relative rise times into absolute distances, we correlated the dendritic location of a conductance with its rise time in voltage-jump experiments (Figures 4E and 4F). When we used TF 2P to activate ChR2 expressed in SPNs (Figures 4E–4I) and measured voltage-jump kinetics of currents evoked at different somatodendritic locations, the two parameters correlated well (Figure 4F). However, beyond ~150 μm from the soma, the currents became too small for accurate analysis (Figure 4I). To gain access to very distal dendrites, we used 2P glutamate uncaging combined with voltage jumps (Figures 4E, 4J, and 4K). We rapidly activated synapses on three neighboring spines (333 Hz; Figure 4K) under conditions that maximized current amplitudes. Again, rise times correlated well with distance of the stimulated spines (Figure 4B) and allowed experimental access to the entire dendrite. Importantly, the TF ChR2 activation and glutamate uncaging revealed the same distance dependence over the jointly probed 50–150 μm distances, confirming the independence of the method on the nature of the current source. To determine the position of synapses formed by LTSIs and FSIs, respectively, we fit the combined data from TF 2P ChR2 activation and 2P glutamate uncaging with a linear regression and overlaid the resulting fit with the 10%–90% distribution of rise times obtained for synaptic currents. This indicates that the soma and most proximal dendritic region (~50 μm) of SPNs are exclusively targeted by FSIs. Following a region where both types of inputs co-exist (~50–100 μm), the major part of SPN dendrites (~100–250 μm) is exclusively targeted by LTSIs (Figure 4F).

DISCUSSION

Here we used optogenetic, electrophysiological, 2P imaging, and viral tracing approaches to determine whether spatial organizing principles exist within striatal microcircuits. We describe a microcircuit in which FSIs form strong synapses only onto the proximal somatodendritic region of nearby SPNs, whereas LTSIs target both SPNs and CINs and form synapses onto distal dendritic regions of spatially distant cells.

The viral tracing experiments were performed in D1R-cre mice, limiting our results to SPNs of the direct pathway. However, given that we found no functional difference in LTSI inputs to the direct and indirect pathway SPNs and that the connection cannot be detected in paired recordings irrespective of the SPN-type (Gittis et al., 2010), it is likely that the conclusion of long-distance synapse formation applies to both pathways.

Since cortico-striatal inputs are organized topographically (Bolam et al., 2000), synaptically connected FSIs and SPNs

Figure 4. Proximal-Distal Distribution of FSI and LTSI Connections onto SPNs

(A) Schematic of voltage-jump experiments: stepping the holding potential (V_h) to apply a stronger driving force increases the amplitude of activated currents. Sites further from the somatic recording electrode take longer to reach the new holding potential (magenta). Thus, onset kinetics of synaptic currents in voltage jumps reflect the proximal-distal location of the synapse.

(B) Example of voltage-jump experiment: under control conditions (V_h constantly −40 mV, gray trace), an IPSC evokes an inward current. When holding the cell initially at 0 mV, activation of the synapse (arrowhead) does not result in a current despite $GABA_A$ receptors being activated (control trace) until a negative holding potential is applied (V_h from 0 mV to −40 mV, blue). Inset shows rise phase of voltage jump superimposed with exponential fit (red).

(C) Current onset in voltage-jump experiments as shown in (B) for all LTSI, FSI, and lateral SPN inputs. Lines indicate average, and shaded areas represent SEM.

(D) Individual rise times for current onset in voltage jumps are slower for LTSI and SPN synapses, indicating a distal dendritic distribution.

(E) Schematic of calibration experiments: two approaches were used to correlate the dendritic location of a conductance with its rise time in voltage-jump experiments. In ChR2-expressing SPNs, TF (940 nm) was used for activation at various locations along a dendrite (top, blue; G–I). Alternatively, 2P uncaging was used to activate glutamatergic synapses (bottom, red; J and K). Both types of currents were combined with voltage-jump recordings.

(F) Summary data from TF-2P ChR2 activation (n = 17 locations/10 cells) and glutamate-uncaging (18/10) experiments. The proximal-distal distance of individual conductances correlated with rise time in voltage jumps. Shaded area: 10%–90% distribution for LTSI (magenta) and FSI inputs (green).

(G) Left: example of a ChR2-expressing SPN. Circles indicate approximate size of the TF laser spot and its location on the soma (1) or next to it (2). Right: ChR2 currents evoked by a 10 ms illumination (cyan bar) at the two locations demonstrate spatial specificity of TF.

(H) Example of a voltage-jump experiment with TF 2P ChR2 activation, analogous to (B), but with ChR2 current as conductance. Light was 12 ms and the voltage step was 10 ms into the stimulus.

(I) Moving TF activation distally quickly reduced current size. Numbers indicate distance from soma.

(J) 2P image of example SPN, arrows indicate three different sites probed by glutamate uncaging.

(K) Left: high-magnification images of sites indicated in (J). Red dots mark uncaging positions, and numbers indicate distance from soma along the dendrite. Middle: voltage-jump experiments for each site; arrowheads indicate uncaging. Right: rise time of voltage jumps correlated with distance of the uncaging site. Bar diagrams represent mean ± SEM; ***$p < 0.0001$, n.s.

See also Figures S3 and S4.

probably share common excitatory inputs, consistent with the proposed function of FSIs in mediating feed-forward inhibition (Tepper et al., 2004). In contrast, spatially separated, but synaptically connected, LTSIs and SPNs likely receive different inputs, and thus LTSIs may organize functional assemblies by mediating lateral inhibition, as do SST-positive interneurons in cortex and hippocampus (Adesnik et al., 2012; Stefanelli et al., 2016). Systematic mapping of the cortico-striatal connectome revealed 29 distinct striatal domains and suggests differentiation into functional modalities (Hintiryan et al., 2016). Interestingly, the viral tracing approach used here reveals that LTSIs (but not FSIs) form synapses onto SPNs up to several millimeters away, well beyond the border of these domains, suggesting that LTSIs contribute to signal processing across functional modalities.

Our finding that SST-positive LTSIs and PV-positive FSIs target distal and proximal dendritic regions, respectively, demonstrates that this organization principle is conserved in striatum. In cortex and hippocampus (e.g., Lovett-Barron et al., 2012; Marlin and Carter, 2014), distal dendrites of projection neurons are found in particular laminae, providing a potential cell-extrinsic cue to direct GABAergic axons. In striatum, there is no macroscopic organization in the arrangement and dendritic morphology of SPNs, indicating that a signal intrinsic to the SPN dendrite must determine the proximal-distal location of GABAergic synapses.

The dendritic targeting of LTSIs also has important functional implications. Dendritic synaptic inhibition can regulate dendritic nonlinear and plastic processes (Llinás et al., 1968; Miles et al., 1996) but also effectively deliver branch-specific shunting of electrical activity (Gidon and Segev, 2012), thereby effectively controlling the output of the target neuron (Lovett-Barron et al., 2012). In the case of SPNs, this is particularly interesting, since SPNs can alternate between a hyperpolarized "down-state" and a depolarized "up-state," with the latter being a prerequisite for spiking activity (Stern et al., 1998). The transition to up-states can be mimicked by concerted activation of multiple excitatory synapses at distal dendrites, starting at ~100 μm from the soma (Plotkin et al., 2011). This coincides with the region that we identify here as targets of LTSI inputs (Figure 4F), raising the intriguing possibility that LTSIs can effectively control SPN spiking by controlling dendritic nonlinearities.

EXPERIMENTAL PROCEDURES

Heterozygous *Somatostatin-cre* (SST-cre) and *Parvalbumin-cre* (PV-cre) knockin mice (Jackson Laboratory) and bacterial artificial chromosome (BAC)-transgenic *Adora2a-cre*, *Drd1a-cre*, and *Drdr2-EGFP* mice (GENSAT) were used.

For electrophysiological analysis, acute parasagittal brain slices were obtained from mice at postnatal days 40–45 (P40–P45). Whole-cell recordings were made at 33°C–34°C from cells in anterior dorsolateral and dorsomedial striatum. $GABA_A$ receptor-mediated currents were pharmacologically isolated as inward currents following chloride loading. ChR2 was activated either by blue (1 ms, 473 nm) or by temporally focused, near-infrared (10 ms, 940 nm) light pulses.

Data are represented as mean ± SEM (bars) superimposed on all individual data points (circles) and were compared using the nonparametric Mann-Whitney test (for group comparisons) or Kruskall-Wallis ANOVA followed by Dunn's test (for multiple group comparisons), unless otherwise noted.

For viral *trans*-synaptic tracing, a cre-dependent lentivirus encoding TVA receptor, B19G rabies glycoprotein, and tdTomato was injected into dorsal striatum of *Drd1a-cre* mice, followed by a pseudotyped rabies virus encoding EGFP 3 weeks later. After 7 days, mice were processed for immunohistochemistry and imaged. The striatum was reconstructed into three dimensions, and the xyz position of each starter cell and monosynaptically connected interneuron was determined.

SUPPLEMENTAL INFORMATION

Supplemental Information includes Supplemental Experimental Procedures, four figures, and one table and can be found with this article online at http://dx.doi.org/10.1016/j.neuron.2016.09.007.

AUTHOR CONTRIBUTIONS

C.S. and B.L.S. conceived of the study, designed experiments, and wrote the manuscript. C.S. and J.L.S. performed experiments with help of D.D.F. A.B. designed and built the temporal focusing microscope. K.W.H. made the rabies virus and advised on its use. All authors commented on the manuscript.

ACKNOWLEDGMENTS

We thank K. Bistrong, N. Wong, and A. Philson for technical support; D. Hochbaum for help with data analysis; and members of the B.L.S. lab for helpful discussions. Lhx6-GFP mice were kindly provided by M. Levine (UCLA). The constructs for generating lentivirus and pseudotyped rabies virus were a gift from B.K. Lim (UCSD). The BCH Core produced lentivirus (P30EY012196). Macros for analysis of the viral tracing experiments were written by L. Ding (Harvard Enhanced Neuroimaging Core). This work was supported by the German Academic Exchange Service/DAAD (C.S.), the Lefler Center for the Study of Neurodegenerative Disorders (C.S.), the Istituto Italiano di Tecnologia (A.B.), the Prix du Jeune Chercheur Fondation Bettencourt Schueller (A.B.), and NIH (NS046579; B.L.S.).

Received: April 1, 2016
Revised: July 11, 2016
Accepted: August 29, 2016
Published: October 5, 2016

REFERENCES

Adesnik, H., Bruns, W., Taniguchi, H., Huang, Z.J., and Scanziani, M. (2012). A neural circuit for spatial summation in visual cortex. Nature *490*, 226–231.

Bakhurin, K.I., Mac, V., Golshani, P., and Masmanidis, S.C. (2016). Temporal correlations among functionally specialized striatal neural ensembles in reward-conditioned mice. J. Neurophysiol. *115*, 1521–1532.

Bennett, B.D., and Bolam, J.P. (1994). Synaptic input and output of parvalbumin-immunoreactive neurons in the neostriatum of the rat. Neuroscience *62*, 707–719.

Bolam, J.P., Hanley, J.J., Booth, P.A., and Bevan, M.D. (2000). Synaptic organisation of the basal ganglia. J. Anat. *196*, 527–542.

DeFelipe, J., Alonso-Nanclares, L., and Arellano, J.I. (2002). Microstructure of the neocortex: comparative aspects. J. Neurocytol. *31*, 299–316.

DiFiglia, M., and Aronin, N. (1982). Ultrastructural features of immunoreactive somatostatin neurons in the rat caudate nucleus. J. Neurosci. *2*, 1267–1274.

Druckmann, S., Feng, L., Lee, B., Yook, C., Zhao, T., Magee, J.C., and Kim, J. (2014). Structured synaptic connectivity between hippocampal regions. Neuron *81*, 629–640.

Gidon, A., and Segev, I. (2012). Principles governing the operation of synaptic inhibition in dendrites. Neuron *75*, 330–341.

Gittis, A.H., and Kreitzer, A.C. (2012). Striatal microcircuitry and movement disorders. Trends Neurosci. *35*, 557–564.

Gittis, A.H., Nelson, A.B., Thwin, M.T., Palop, J.J., and Kreitzer, A.C. (2010). Distinct roles of GABAergic interneurons in the regulation of striatal output pathways. J. Neurosci. *30*, 2223–2234.

Harris, K.D., and Shepherd, G.M. (2015). The neocortical circuit: themes and variations. Nat. Neurosci. *18*, 170–181.

Hintiryan, H., Foster, N.N., Bowman, I., Bay, M., Song, M.Y., Gou, L., Yamashita, S., Bienkowski, M.S., Zingg, B., Zhu, M., et al. (2016). The mouse cortico-striatal projectome. Nat. Neurosci. *19*, 1100–1114.

Ibáñez-Sandoval, O., Tecuapetla, F., Unal, B., Shah, F., Koós, T., and Tepper, J.M. (2011). A novel functionally distinct subtype of striatal neuropeptide Y interneuron. J. Neurosci. *31*, 16757–16769.

Ito, M. (2006). Cerebellar circuitry as a neuronal machine. Prog. Neurobiol. *78*, 272–303.

Kawaguchi, Y. (1993). Physiological, morphological, and histochemical characterization of three classes of interneurons in rat neostriatum. J. Neurosci. *13*, 4908–4923.

Kawaguchi, Y., Wilson, C.J., and Emson, P.C. (1990). Projection subtypes of rat neostriatal matrix cells revealed by intracellular injection of biocytin. J. Neurosci. *10*, 3421–3438.

Kita, H., Kosaka, T., and Heizmann, C.W. (1990). Parvalbumin-immunoreactive neurons in the rat neostriatum: a light and electron microscopic study. Brain Res. *536*, 1–15.

Koos, T., Tepper, J.M., and Wilson, C.J. (2004). Comparison of IPSCs evoked by spiny and fast-spiking neurons in the neostriatum. J. Neurosci. *24*, 7916–7922.

Kubota, Y., and Kawaguchi, Y. (2000). Dependence of GABAergic synaptic areas on the interneuron type and target size. J. Neurosci. *20*, 375–386.

Llinás, R., Nicholson, C., Freeman, J.A., and Hillman, D.E. (1968). Dendritic spikes and their inhibition in alligator Purkinje cells. Science *160*, 1132–1135.

London, M., and Häusser, M. (2005). Dendritic computation. Annu. Rev. Neurosci. *28*, 503–532.

Lovett-Barron, M., Turi, G.F., Kaifosh, P., Lee, P.H., Bolze, F., Sun, X.H., Nicoud, J.F., Zemelman, B.V., Sternson, S.M., and Losonczy, A. (2012). Regulation of neuronal input transformations by tunable dendritic inhibition. Nat. Neurosci. *15*, 423–430, S1–S3.

MacAskill, A.F., Little, J.P., Cassel, J.M., and Carter, A.G. (2012). Subcellular connectivity underlies pathway-specific signaling in the nucleus accumbens. Nat. Neurosci. *15*, 1624–1626.

Marlin, J.J., and Carter, A.G. (2014). GABA-A receptor inhibition of local calcium signaling in spines and dendrites. J. Neurosci. *34*, 15898–15911.

Miles, R., Tóth, K., Gulyás, A.I., Hájos, N., and Freund, T.F. (1996). Differences between somatic and dendritic inhibition in the hippocampus. Neuron *16*, 815–823.

Pearce, R.A. (1993). Physiological evidence for two distinct GABAA responses in rat hippocampus. Neuron *10*, 189–200.

Petreanu, L., Mao, T., Sternson, S.M., and Svoboda, K. (2009). The subcellular organization of neocortical excitatory connections. Nature *457*, 1142–1145.

Plotkin, J.L., Day, M., and Surmeier, D.J. (2011). Synaptically driven state transitions in distal dendrites of striatal spiny neurons. Nat. Neurosci. *14*, 881–888.

Redgrave, P., Vautrelle, N., and Reynolds, J.N. (2011). Functional properties of the basal ganglia's re-entrant loop architecture: selection and reinforcement. Neuroscience *198*, 138–151.

Roux, L., and Buzsáki, G. (2015). Tasks for inhibitory interneurons in intact brain circuits. Neuropharmacology *88*, 10–23.

Sanes, J.R., and Zipursky, S.L. (2010). Design principles of insect and vertebrate visual systems. Neuron *66*, 15–36.

Stefanelli, T., Bertollini, C., Lüscher, C., Muller, D., and Mendez, P. (2016). Hippocampal somatostatin interneurons control the size of neuronal memory ensembles. Neuron *89*, 1074–1085.

Stern, E.A., Jaeger, D., and Wilson, C.J. (1998). Membrane potential synchrony of simultaneously recorded striatal spiny neurons in vivo. Nature *394*, 475–478.

Straub, C., Tritsch, N.X., Hagan, N.A., Gu, C., and Sabatini, B.L. (2014). Multiphasic modulation of cholinergic interneurons by nigrostriatal afferents. J. Neurosci. *34*, 8557–8569.

Szydlowski, S.N., Pollak Dorocic, I., Planert, H., Carlén, M., Meletis, K., and Silberberg, G. (2013). Target selectivity of feedforward inhibition by striatal fast-spiking interneurons. J. Neurosci. *33*, 1678–1683.

Tepper, J.M., Koós, T., and Wilson, C.J. (2004). GABAergic microcircuits in the neostriatum. Trends Neurosci. *27*, 662–669.

Xu-Friedman, M.A., and Regehr, W.G. (1999). Presynaptic strontium dynamics and synaptic transmission. Biophys. J. *76*, 2029–2042.

Zhu, G., van Howe, J., Durst, M., Zipfel, W., and Xu, C. (2005). Simultaneous spatial and temporal focusing of femtosecond pulses. Opt. Express *13*, 2153–2159.